Iterative Spectral Unmixing for Optimizing Per-Pixel Endmember Sets

Derek M. Rogge, Benoit Rivard, Jinkai Zhang, and Jilu Feng

***Abstract*—Fractional abundances predicted for a given pixel using spectral mixture analysis (SMA) are most accurate when only the endmembers that comprise it are used, with larger errors occurring if inappropriate endmembers are included in the unmixing process. This paper presents an iterative implementation of SMA (ISMA) to determine optimal per-pixel endmember sets from the image endmember set using two steps: 1) an iterative unconstrained unmixing, which removes one endmember per iteration based on minimum abundance and 2) analysis of the root-mean-square error as a function of iteration to locate the critical iteration defining the optimal endmember set. The ISMA was tested using simulated data at various signal-to-noise ratios (SNRs), and the results were compared with those of published unmixing methods. The ISMA method correctly selected the optimal endmember set 96% of the time for SNR of 100 : 1. As a result, per-pixel errors in fractional abundances were lower than for unmixing each pixel using the full endmember set. ISMA was also applied to Airborne Visible/Infrared Imaging Spectrometer hyperspectral data of Cuprite, NV. Results show that the ISMA is effective in obtaining abundance fractions that are physically realistic (sum close to one and nonnegative) and is more effective at selecting endmembers that occur within a pixel as opposed to those that are simply used to improve the goodness of fit of the model but not part of the mixture.**

***Index Terms*—Data processing, optimization methods, remote sensing, spectral analysis.**

I. Introduction

In HYPERSPECTRAL imagery, the spectral signature of each pixel commonly comprises the combined measured reflectance of components within the sensor's field of view. Spectral mixing is a problem inherent to remote sensing data, and as a result, few image pixels are spectrally "pure" [1], which complicates spectral identification and classification. This problem can be addressed by linear spectral mixture analysis (SMA), which classifies mixed pixels [2], [3] by deconvolving (unmixing) each pixel spectrum into fractional abundances of its surface constituents or endmember spectra. Applying the linear SMA to a given mixture requires that endmembers occur as spatially segregated patterns [4] with a multiple scattering involving several endmembers (nonlinear mixing) being negligible. If this requirement is met, and the endmembers and their spectral signatures are known, linear SMA can be used to estimate fractional abundances for each pixel using approaches such as, the maximum-likelihood setup [5], constrained least-squares [6], using endmember bundles to address endmember spectral variability [7], and using multiple endmember SMA (MESMA), which addresses per-pixel endmember variability [8]. Examples of the application of the linear SMA can be found in studies by [9]–[14].

Commonly endmember spectra used for linear SMA are selected from image data because: 1) available library and field spectra were not necessarily acquired under the same conditions as airborne or satellite image data; 2) important surface components may not be adequately represented in spectral libraries; and 3) image endmembers have the advantage of being directly associated with surface components detectable in the scene. Selection of image endmembers that are good representations of surface components is necessary for accurate unmixing. As such, a number of image endmember extraction tools have been developed and include a pixel purity index (PPI) [15], manual endmember selection tool (MEST) [16], N-FINDR [17], optical real-time adaptive spectral identification system (ORASIS) [18], convex cone analysis (CCA) [19], iterative error analysis (IEA) [20], automated morphological endmember extraction (AMEE) [21], iterated constrained endmembers (ICE) [22], and vertex component analysis (VCA) [23].

Typically, the linear SMA is applied to each pixel using the endmember set obtained from the full image. The number of endmembers in this set can vary substantially [24] depending on the spectral complexity of a scene, the spatial scale, spectral resolution, and the number of bands in the image. Commonly, this number is greater than the number of endmembers required to unmix a single pixel in the scene. Abundances predicted using linear SMA are most accurate when only the endmembers that comprise a given pixel are used, with larger abundance errors occurring when either too few or too many endmembers are used [6], [25]. Fractional abundance errors owing to an excess of endmembers can be reduced if the image endmember set can be optimized on a per-pixel basis, where this optimized endmember subset or pixel endmember set is more representative for the given pixel. Adopting linear SMA to account for variability in the number of endmembers on a per-pixel basis is the focus of this paper and should not be confused with the endmember spectral variability, which is addressed in papers by Bateson *et al.* [7] and Petron and Foschi [26].

To account for variability in the number of endmembers on a per-pixel basis, the method presented in this paper makes use of an iterative SMA (ISMA) to optimize the image endmember set on a per-pixel basis. We first apply the ISMA to a simulated image comprising randomly generated mineral mixtures

Manuscript received January 16, 2006; revised April 27, 2006. This work was supported by the GEOmatics for Informed DEcisions (GEOIDE) Network of Centres of Excellence of Canada and the National Science and Engineering Research Council of Canada.

The authors are with the Earth Observation Systems Laboratory, Department of Earth and Atmospheric Sciences, University of Alberta, Edmonton, AB T6G 2E3, Canada (e-mail: benoit.rivard@ualberta.ca).

Digital Object Identifier 10.1109/TGRS.2006.881123

generated with a known image endmember set and with a range of signal-to-noise ratios (SNRs). The use of simulated data allows us to directly determine the accuracy of the per-pixel sets predicted. The results show that the ISMA can effectively select the most appropriate endmember set for each pixel. This, in turn, results in more accurate abundance estimations than achieved when the full image endmember set is used to unmix every pixel. Finally, we apply the ISMA to a real hyperspectral data set collected by the Airborne Visible/Infrared Imaging Spectrometer (AVIRIS) sensor over Cuprite, NV.

II. Background

Linear spectral mixture analysis is based on the premise that a given mixture can be modeled using a set of linearly independent endmember spectra. To deconvolve a spectrum into fractional abundances of its constituent endmember spectra, the following equation can be solved using a least squares approach:

$$R_b = \sum_{i=1}^{n} F_i S_{ib} + E_b \tag{1}$$

where R_b is the reflectance of the pixel at band b, F_i is the fractional abundance of the endmember i, S_{ib} describes the reflectance of endmember i at band b, n equals the number of endmembers, and E_b is the error of the fit at band b. The least squares estimator used to solve (1) can generate fractional abundances that are positive and negative. In this case, the linear unmixing solution is said to be unconstrained and is computationally simplistic. Unconstrained unmixing is particularly sensitive to the use of endmembers that are not part of the given mixture, resulting in solutions that are not physically realistic (e.g., negative fractions). If constraints are imposed, such that fractional abundances sum-to-one (ASC), and fractional abundances are nonnegative (ANC), unmixing is computationally more complex. The simultaneous implementation of ASC and ANC is usually recommended to produce fractional abundances that are physically realistic [6]. The root-mean-square (rms) error representing the "goodness of fit" for the modeled spectrum compared to the image spectrum can be calculated as

$$\text{rms} = \left(\frac{\sum_{b=1}^{k} (r_b - p_b)^2}{k} \right)^{\frac{1}{2}} \tag{2}$$

where r_b and p_b are the modeled and image spectrum values at band b, respectively. k is the number of bands.

The concept of unmixing each pixel based on an optimal per-pixel endmember set has been presented in papers such as, [3], [8], and [27]–[29]. In [3] and [27], the authors made use of the spatial association of pixels to that of endmembers in the image, and in [28], a hierarchical and stepwise spectral unmixing was presented. In [8] and [29], the unmixing process was used to determine which endmembers from a candidate endmember set are most appropriate to unmix a given mixture. The MESMA described in [8] made use of a candidate endmember set comprising spectra of vegetation and soils measured in the field and laboratory. For each pixel, the MESMA examined all possible combinations of models of two and three endmembers from the candidate endmember set. Endmember models were retained if they met three criteria: 1) the rms error was below a preset threshold; 2) the unmixing model had physically reasonable fractions between -0.01 and 1.01; and 3) each band residual did not exceed a predetermined threshold. It is possible that more than one endmember model can meet the three criteria of MESMA. This warrants additional steps to determine which of the combinations is most appropriate. In [8], a subset of models was selected, which provided an optimal areal coverage. A problem arising from this approach is that multiple fractional output maps can result from models with different numbers of endmembers. In [30] and [31], a different approach was suggested, whereby the endmember model with the lowest rms error would be retained. This approach is reasonable if the number of endmembers are fixed for each model [30]. However, if the number of endmembers is to be variable, then the minimum rms error cannot be used. This is because, as additional endmembers are added to the model, the rms error will decrease, even if the endmember is not in the mixture [29]–[31]. To address this problem, Li and Mustard [31] suggested that the model with the fewest endmembers should be used if the rms error is lower than the noise. In [32], the higher order endmember model is retained if the rms error is 0.8% lower for models with more endmembers. Evaluating all possible combinations, verifying if each model meets the three criteria, and determining which of the candidate endmember models is optimal make the MESMA computationally intensive [8], [30]–[35].

In [29], high-resolution laboratory thermal emission spectra were used to test a number of factors that affect the applicability of the SMA, notably blind endmember input. It was recognized that endmembers with negative fractional abundances are physically unrealistic and likely not part of the mixture. Thus, their approach was to remove all endmembers with negative abundance fractions and repeat the unmixing process on the remaining endmember set until no negative abundances remain. This iterative approach is computationally less intensive than the MESMA, but it cannot detect endmembers with positive fractions that are not part of the mixture. ISMA is an alternative approach that integrates the iterative concepts used in [29] and the change in rms as a function of the number of endmembers [29]–[32]. The method does not require an examination of all possible endmember combinations, thereby reducing the computational complexity, and it can remove endmembers with positive as well as negative abundances that are not part of a mixture, thus obtaining the optimal per-pixel endmember set. The following section describes the ISMA.

III. ISMA

Once an image endmember set has been determined using one of the endmember extraction methods listed in Section I, the ISMA can be implemented to determine the optimal per-pixel endmember set and produce fractional abundance images for each endmember. To account for changes in the geometry of incident light caused by topography, a shade endmember was

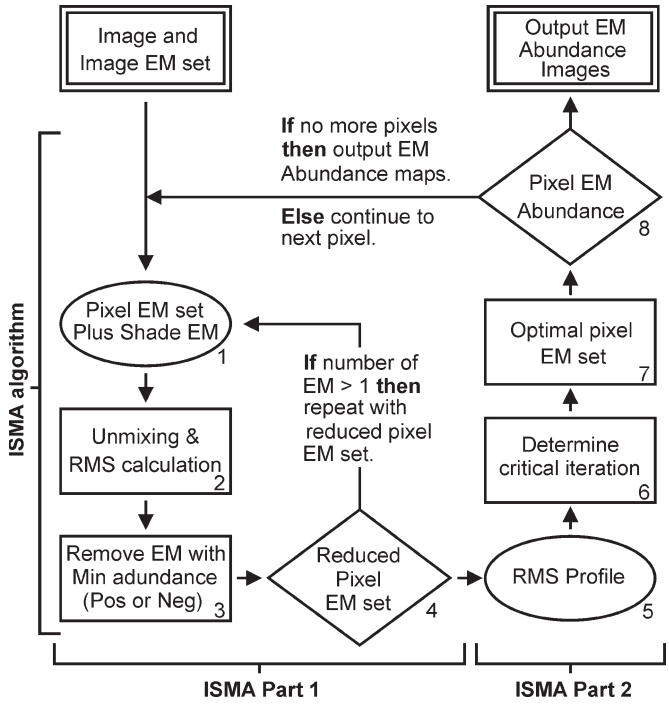

Fig. 1. Schematic representation of the ISMA. Input data sets include the hyperspectral image and the derived image endmember set. Steps 1 through 8 are applied pixel by pixel. Part 1 (steps 1 through 4) of the ISMA iteratively removes the endmembers from the pixel endmember set based on minimum abundance until only one endmember and shade remain. Part 2 (steps 5 through 8) of the ISMA determines the critical iteration from the rms profile generated in Part 1. The optimal pixel endmember set is used to unmix the given pixel spectrum, with results for all pixel output as endmember fractional abundance images.

used in [2], [4], [8], and [10]. In [8], a uniform reflectance shade endmember was used, which can be considered a neutral multiplicative scaling factor [4]. For the ISMA, a shade endmember is also included with the image endmember set as it is assumed that each mixture has some degree of shade. For each pixel in the image, the implementation of the ISMA is in two parts: 1) iterative unmixing to remove endmembers one at a time and 2) determining the optimal endmember set by analyzing the change in rms as a function of the number of endmembers (Fig. 1). The first step of part 1) is to apply unconstrained linear unmixing using the pixel endmember set (step 2, Fig. 1). From the unconstrained unmixing solution, the endmember with the lowest abundance (positive or negative) is removed excluding the shade endmember, which is retained for all iterations (step 3, Fig. 1). If the number of pixel endmembers remaining is > 1 excluding the shade endmember, a new unmixing solution is calculated with the remaining endmembers. The process is repeated until one endmember and the shade endmember remain. Unconstrained unmixing is used instead of constrained unmixing, because as the endmember set for a given mixture approaches the endmembers that actually comprise it, the predicted abundances should be similar to the actual abundances and should sum close to one.

The second part of the ISMA involves an examination of the change in the rms error over all iterations to determine the critical iteration that uses too few endmembers (steps 5–7, Fig. 1). The rms error should be variable but low, as long as the actual endmembers that comprise the mixture have not been discarded. However, once one of the actual endmembers is removed during the iterative process, the rms will increase substantially because too few endmembers are available to effectively model the mixture. This is the critical iteration and is determined automatically by calculating the change in the rms error (Δrms) starting from the last iteration until Δrms is below a preset threshold. Δrms is calculated as

$$\Delta\text{rms} = 1 - (\text{rms}_{\text{it}-1}/\text{rms}_{\text{it}}) \tag{3}$$

where rms_{it} is the nth iteration rms value. The search process begins with the last iteration because: 1) the actual number of endmembers necessary to unmix each mixture is likely much smaller than the maximum available and can be reached quickly; and 2) minor rms variability observed for the first few iterations may exceed the Δrms threshold and prematurely stop the process. ISMA also requires the Δrms value to be below the threshold for a predetermined number of successive iterations before the process is halted. The optimal endmember set is then determined to be the first of these successive iterations and is used to calculate the pixel fractional abundances (step 8, Fig. 1). The final outputs are endmember fractional abundance images.

For the ISMA, the maximum number of necessary unmixing iterations per pixel is defined by the endmember set. For example, a set of ten image endmembers would require ten unmixing iterations per pixel. In comparison, 375 unmixing calculations would be required for each pixel to test all possible two-, three-, and four-endmember combinations using the MESMA. If the candidate endmember set becomes larger, the number of unmixing calculations for ISMA increases linearly, whereas for MESMA, the number increases significantly faster.

IV. Testing Methodology

To assess the applicability of the ISMA, we first examine the accuracy of the selected optimal endmember set and the resulting fractional abundances for simulated data described in the next section. For this data set, per-pixel endmember sets and fractional abundances are known, since they are used to generate the mixed spectrum of each pixel, thus enabling a direct comparison with estimated pixel endmember sets and abundances. The average fractional abundance error (f_{avg}) is calculated as

$$f_{\text{avg}} = \frac{\sum_{i=1}^{m}\sum_{j=1}^{n}|a_j - e_j|}{m} \tag{4}$$

where n is the number of endmembers, m is the number of mixtures in the image, and a_j and e_j are the actual and estimated fractions for endmember j, respectively. The number of endmembers in (4) can be variable, such that f_{avg} can be calculated for a group or a single endmember. Equation (4) can also be adjusted for m, such that f_{avg} can be calculated for simulated mixtures that comprise any number of mixtures. Errors in the fractional abundances estimated with the ISMA are then compared with those obtained from least squares unconstrained and constrained unmixing using all available

image endmembers and using the approach in [29]. The fully constrained unmixing approach in [36] was implemented using the imaging spectrometer data-analysis system (ISDAS) [37]. A direct comparison with the MESMA is not warranted as it will be demonstrated that the ISMA can effectively select the correct per-pixel endmember sets and obtain accurate abundance fractions without the computational complexity of MESMA.

A second test is presented using AVIRIS hyperspectral data for Cuprite, NV, an area where spectral endmembers have been reasonably well documented (e.g., [38]), but where fractional abundances are not known. To asses the fractional abundance maps generated using the ISMA, results should be physically realistic: 1) sum to one and 2) be nonnegative. Histograms of the distribution of fractional abundances for individual endmembers and for pairs of endmembers are analyzed. These are compared with the results from a fully constrained unmixing using all available endmembers.

V. Hyperspectral Data Sets

A. Simulated Data Set

The simulated data set comprises 10 000 random linear mixtures generated from 29 mineral spectra obtained from the U.S. Geological Survey (USGS) spectral library [39] and a shade spectrum (Table I). The 420 bands of each spectrum span 0.4 to 2.56 μm with an average spectral resolution of 0.005 μm ($\sim$0.002 in the visible to $\sim$0.01 in the short-wave infrared). Spectra for common rock-forming minerals were chosen including multiple spectra for actinolite, calcite, goethite, kaolinite, and muscovite (Table I). The latter were used to test the robustness of the methodology to minor spectral variations of the same mineral.

For each mixture, the combination of endmembers was randomly chosen. A shade endmember with a uniform reflectance was included in all mixtures (1% of absolute reflectance). The simulated data have an average number of $\sim$3.5 endmembers for all mixtures. The minimum and maximum number of endmembers for the mixtures are 1 and 12, respectively (excluding the shade endmember). The mixtures generated are mathematically correct but are not necessarily geologically realistic (e.g., occurrence of magnesium-rich olivine and quartz).

Noise was added to the random mixtures using a standard normal distribution of randomly generated numbers. SNRs of 12 : 1, 25 : 1, 50 : 1, and 100 : 1 were used assuming a 50% absolute reflectance. The outcome was four data sets, each containing 10 000 mixtures at a specific SNR. The noise was added using the following equation:

$$r'_b = r_b + \left(M * \left(\frac{q(0,1)}{\text{SNR}} \right) \right) \tag{5}$$

where r is the reflectance, q is a randomly generated number with a mean of zero and a standard deviation of one, and M is the assumed reflectance for the spectrum. For example, if the reflectance is given as a value between zero and one, we can assign an additive noise based on an assumed reflectance of 50% or $M = 0.5$. The SNR values used in this paper are consistent with those used by Chang *et al.* [19], [40], who used simulated data to test the constrained unmixing methods with the SNR ranging from 5 : 1 to 40 : 1; and Plaza *et al.* [21] who used SNR of 10 : 1 to 110 : 1 to test endmember extraction algorithms. When we test the unmixing approaches with this data set, we use the same endmember set as used for the creation of the simulated mixtures (Table I).

TABLE I
List of Endmember Spectra (From USGS Spectral Library [39]) Used to Generate the Simulated Data Set. Minerals With Multiple-Endmember (EM) Spectra Are in Bold

EM no.	Library Name	Mineral Name	Library Details
1	**actinol1.spc**	**Actinolite**	**HS116.3B**
2	**actinol3.spc**	**Actinolite**	**HS315.4B**
3	albite3.spc	Albite	HS66.3B
4	almand1.spc	Almandine	HS114.3B
5	alunite1.spc	Alunite	GDS84 Na03
6	anorthi2.spc	Anorthite	HS201.3B
7	budding1.spc	Buddingtonite	GDS85 D-206
8	**calcite1.spc**	**Calcite**	**WS272**
9	**calcite2.spc**	**Calcite**	**HS48.3B**
10	chlorit5.spc	Chlorite	SMR-13.d 30-45um
11	dickite1.spc	Dickite	NMNH106242
12	epidote2.spc	Epidote	GDS26.b <75um
13	**goethi t3.spc**	**Goethite**	**WS219 (limonite)**
14	**goethi t4.spc**	**Goethite**	**WS220**
15	hematit2.spc	Hemat ite	GDS27
16	hornble1.spc	Hornblende_Mg	NMNH117329
17	**kaolini1.spc**	**Kaolinite**	**CM9**
18	**kaolini8.spc**	**Kaolinite**	**CM7**
19	montmor1.spc	Mont morillonite	SWy-1
20	**muscovi1.spc**	**Muscovite**	**GDS107**
21	**muscovi2.spc**	**Muscovite**	**GDS108**
22	olivine1.spc	Olivine	NMNH137044.a 160u
23	opal2.spc	Opal	TM8896 (hyalite)
24	quartz2.spc	Quartz	GDS31 0-74um fr
25	sphaler4.spc	Sphalerite	S26-34
26	sulfur.spc	Sulfur	GDS94 Reagent
27	talc1.spc	Talc	GDS23 74-250um fr
28	tremoli1.spc	Tremolite	HS18.3
29	zoisite.spc	Zoisite	HS347.3B
30	dark	1% of absolute reflectance	

B. AVIRIS Cuprite Hyperspectral Data Set

The AVIRIS sensor has 224 channels over the 0.37- to 2.51-μm spectral range with an average spectral resolution of $\sim$10 nm. We use a 500 $\times$ 500 pixel subset of the June 19, 1997 Cuprite calibrated data set available from the USGS. This data set has an average SNR of 100 : 1 at most wavelengths [41]. Of the 224 atmospherically corrected channels, we use 167 over the 0.4- to 2.42-μm spectral range. Channels not used are primarily associated with H_2O and OH absorption features near 1.4 and 1.9 μm.

VI. Results

A. Example for One Mixture

For the simulated data multiple Δrms values over successive iterations were tested, with a Δrms threshold of 5% over

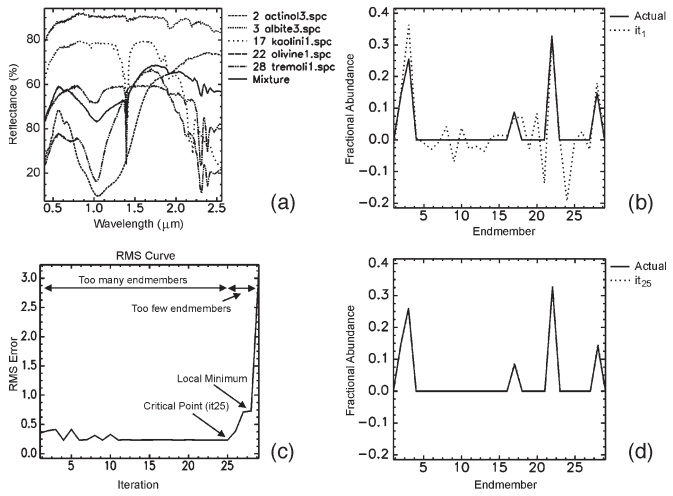

Fig. 2. Graphical representation of the rms error as a function of the number of iterations for (a) mixture of five endmembers showing critical point at iteration 25 (it_{25}) and (c) local minima at $\mathrm{it}_{27}-\mathrm{it}_{28}$. Note the rms variability for the early iterations where an excess of endmembers is used to unmix the given mixture. (b) and (d) show a comparison between the actual endmember abundance (solid line) and the estimated abundance for it_1 (all endmembers) and it_{25} (critical point), respectively. Note the negative and false positive abundances in (b) for the endmember set used in it_1, which is equivalent to the results from an unconstrained unmixing using the 29 available endmembers and shade listed in Table I. Note that the abundances using the endmembers at (d) it_{25} are within < 0.01 of the actual fractions and sum to 0.98.

two successive iterations giving the best results. Fig. 2 shows the spectrum of a single mixture and the spectra of the five-endmember mineral spectra at an SNR of 500 : 1 [Fig. 2(a)] that comprise it. The first unmixing iteration (it_1) with the ISMA uses the 29 endmembers listed in Table I as image endmembers plus shade. Fractional abundances for each endmember for it_1 are shown in Fig. 2(b). Although there is a reasonable estimation of the abundances for the actual endmembers comprising the mixture, the endmembers that are not part of the mixture have positive and negative abundances. The rms error is calculated for it_1 [Fig. 2(c)], which is followed by the removal of the endmember with the lowest abundance, in this case, endmember 24 [refer to Fig. 2(b)]. The process continues until one endmember remains excluding shade. Given the iterative nature of the ISMA, erroneous endmembers are removed first, and those endmembers that comprise the mixture are retained. Examination of the change in rms error through all iterations [Fig. 2(c)] shows that the rms is relatively stable until it_{25}. After it_{25}, the endmembers that comprise the actual mixture begin to be removed, and the rms error increases substantially. Iteration 25 is labeled the critical point on Fig. 2(c) and marks the critical iteration between having too many and too few endmembers, which defines the optimal endmember set for the mixture. Requiring Δrms to be below the given threshold for two successive iterations ensures that the critical point is not mistaken as it_{28}, a local minimum. A comparison of the predicted abundances at it_1 [Fig. 2(b), 30 endmembers] and it_{25} [Fig. 2(d), critical point with optimal set of five endmembers plus shade] illustrates the impact of an appropriate selection of endmembers on the error in endmember fractional abundance. The fractional abundances at it_{25} are within 0.01 of the actual abundances and sum to 0.98.

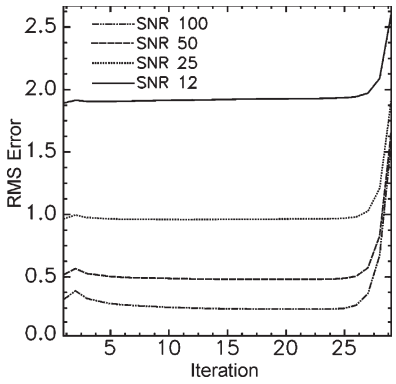

Fig. 3. Average rms profile for all mixtures at SNRs of 100 : 1, 50 : 1, 25 : 1, and 12 : 1. On average, each pixel can be effectively modeled with three to four endmembers.

B. Results for Simulated Data

1) RMS Profile Characteristics: Fig. 3 displays the average rms error as a function of iteration for all mixtures at each SNR. This figure illustrates the consistent characteristics (e.g., critical point) of the rms profiles. The profiles show that the predicted average number of endmembers required to unmix each mixture is between three and four, which is consistent with the actual average for the simulated data sets. The profiles for the individual mixtures have three principal characteristics: 1) minor rms variability over the first few iterations; 2) stable rms over the midrange iterations until the critical point; and 3) substantial increase in rms after the critical point. We observe two exceptions to the characteristic rms error profile: 1) instances with no substantial increase in rms and 2) a local minimum after the rms increases substantially [refer to Fig. 2(c)]. The first case is observed for mixtures that comprise only one endmember. The second may be attributed to the order of endmember removal and the actual abundance fraction of a given endmember to the mixture.

2) Proportion of Correctly Selected Endmembers: For each mixture, the endmembers selected by the ISMA and the method used in [29] are compared with the actual endmembers used in the simulation, and a proportion of correctly selected endmembers calculated $(\text{proportion correct} = \#\text{correct}/\#\text{selected})$. At high SNR (100 : 1), the average proportion of correctly selected endmembers for all mixtures was 96% using ISMA (Table II). This value drops to 83.8% at an SNR of 12 : 1. The method used in [29] resulted in values ranging from 46.3% to 38.9% for these SNR values. On average, the number of endmembers underestimated by the ISMA was 0.24 to 1.31 at SNR of 100 : 1 and 12 : 1, respectively. The method used in [29] fared more poorly and overestimated the actual number of endmembers by a factor of two at each SNR. For both methods, the number of endmembers missed increases with a decreasing SNR. Unconstrained and fully constrained unmixing methods are not included in Table II, as each uses all 30 endmembers to process the data.

3) Average Fractional Abundance Errors: Equation (4) was used to calculate the average fractional abundance error (f_{avg}) for the simulated data at each SNR, where $n = 29$ (all endmembers excluding shade) and $m = 10\,000$ (all pixels). ISMA resulted in lower f_{avg} at all SNR compared with the method

TABLE II
AVERAGE NUMBER OF ENDMEMBERS SELECTED, PROPORTION CORRECTLY SELECTED, AND AVERAGE NUMBER OF ENDMEMBERS MISSED FOR ISMA AND THE METHOD GIVEN IN [29]. VALUES ARE REPORTED AS AVERAGES FOR ALL MIXTURES AT A GIVEN SNR

	ISMA			R&C, 1998		
SNR	# selected	proportion correct	# missed	# selected	proportion correct	# missed
100	3.23	96.0	0.32	7.20	46.3	0.17
50	3.02	94.1	0.61	7.04	44.8	0.35
25	2.65	90.7	1.06	6.67	42.8	0.67
12	2.16	83.8	1.67	6.14	38.9	1.13

Actual average number of endmembers = 3.47

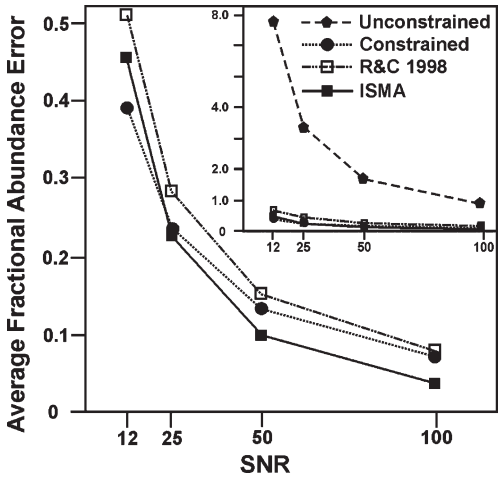

Fig. 4. Average fractional abundance error between the actual and estimated abundances for all endmembers and pixels calculated for the method used in [29]; constrained and unconstrained (inset) unmixing using all 30 endmembers; and the ISMA.

used in [29] and fully constrained unmixing with the exception of constrained unmixing at an SNR of 12 : 1 (Fig. 4). All three methods have average fractional abundance errors that are significantly less than that of the unconstrained unmixing method at all SNR (Fig. 4 inset). The results demonstrate the impact of unmixing using the correct endmembers for each mixture.

When f_{avg} is calculated for each endmember ($n = 1$, $m = 10\,000$), the average fractional abundance error for all mixtures shows a dependence with respect to the given endmember (Fig. 5). The largest error is observed for endmembers with few or no spectral features (#3 albite, #6 anorthite, and #24 quartz) (Fig. 6). This is consistent with least squares theory in that in cases where endmembers are similar or featureless, the endmember matrix will be ill conditioned. For these three endmembers, the results do not enable the selection of a better method among the constrained, ISMA, or the method used in [29]. Endmembers with numerous spectral features consistently display a low fractional abundance error (e.g., #4 almandine, #5 alunite, and #29 zoisite). These endmembers have a lower error for the ISMA than for the fully constrained approach and the method used in [29]. Similar characteristics are observed for the three methods at all SNR investigated, with errors increasing as the SNR decreases.

At a SNR of 100 : 1, the sum of fractional abundances obtained from the ISMA ranged from 0.95–1.05 for 89% of the mixtures, and this value fell to 76%, 58%, and 37% at SNRs of 50 : 1, 25 : 1, and 12 : 1, respectively (Fig. 7). The number

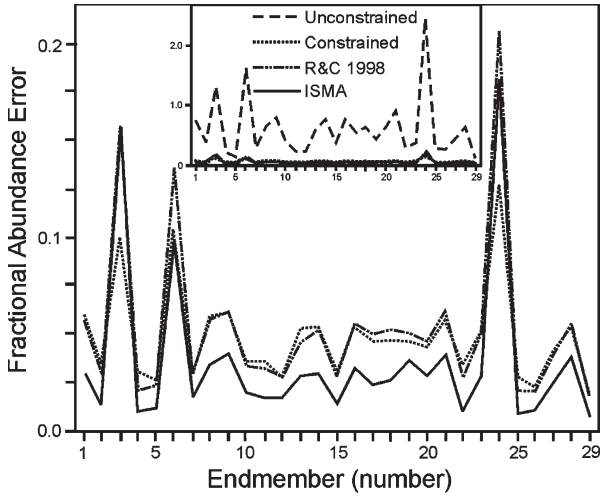

Fig. 5. Average fractional abundance error at an SNR of 50 : 1 for each endmember for all mixtures for the method used in [29]; constrained and unconstrained unmixing using all endmembers; and the ISMA. The inset includes the results for the unconstrained unmixing approach (refer to Table I for the mineral corresponding to the endmember number).

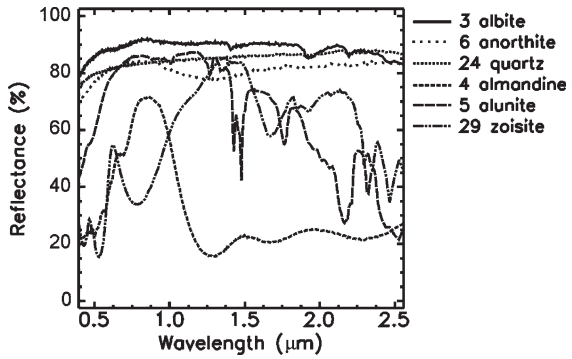

Fig. 6. Selection of endmember spectra with differing spectral contrast. Endmembers with numerous spectral features (almandine, alunite, and zoisite) result in low fractional abundance errors (Fig. 5), whereas high fractional abundance error is associated with endmembers with few spectral features (albite, anorthite, and quartz).

of mixtures that had negative fractional abundances was nine, six, seven, and seven for data sets with SNR of 100 : 1, 50 : 1, 25 : 1, and 12 : 1, respectively. Of these, only one mixture showed a negative fractional abundance exceeding 0.01. These results show that the ISMA can produce physically realistic abundance fractions for the majority of pixels by correctly selecting per-pixel endmember sets, particularly at higher SNR. This is accomplished without the need to impose abundance nonnegative and sum-to-one constraints (ANC and ASC).

4) Dependency of the Error on the Number of Endmembers in the Mixture: Fig. 8 shows the average fractional abundance error as a function of the number of endmembers in the simulated mixtures. Pixels that comprise 10, 11, and 12 endmembers were excluded from this analysis because they are represented by too few mixtures (seven, two, and one, respectively). For the constrained unmixing method and the ISMA, f_{avg} increases as more endmembers are included in the mixture. For the unconstrained unmixing method, the error remains stable [Fig. 8(a) inset] but is significantly larger than for the other two methods. At higher SNR, the ISMA performs better than

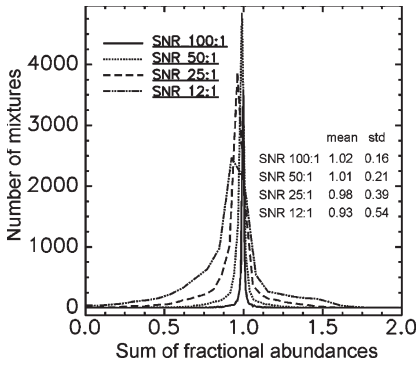

Fig. 7. Histogram distribution of the sum of fractional abundances obtained from the ISMA for each of the 10 000 mixtures at SNRs of 100 : 1, 50 : 1, 25 : 1, and 12 : 1.

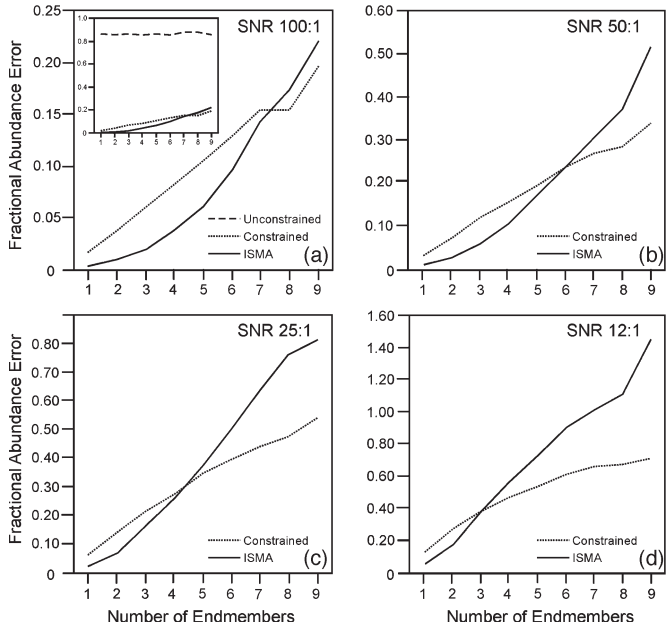

Fig. 8. Average fractional abundance error as a function of the number of endmembers in a given mixture for SNR of (a) 100 : 1, (b) 50 : 1, (c) 25 : 1, and (d) 12 : 1. Unconstrained unmixing included in inset of (a) for an SNR of 100 : 1.

the constrained unmixing method when fewer than seven endmembers comprise a mixture with half the error when mixtures comprise 3–5 endmembers. At an SNR of 12 : 1, the only improvement observed is for mixtures with fewer than three endmembers. For both methods, the lowest error occurs if a single endmember comprises the mixture regardless of the SNR. These results clearly demonstrate the direct influence of the number of endmembers on the predicted fractional abundances.

5) Dependence of the Error on Multiple Endmembers for the Same Mineral: The average fractional abundance errors obtained from the constrained and ISMA methods were compared for mixtures that included multiple endmembers of the same mineral (e.g., muscovi1.spc and muscovi2.spc). Overall, the constrained unmixing method resulted in lower fractional abundance errors than the ISMA method at low SNR ($< 50 : 1$). At higher SNR, the difference in the errors between both methods was small and on the order of 0–0.01 (Fig. 9). For the ISMA method, the highest errors occur when one or both of the similar endmembers have low fractional abundance (e.g.,

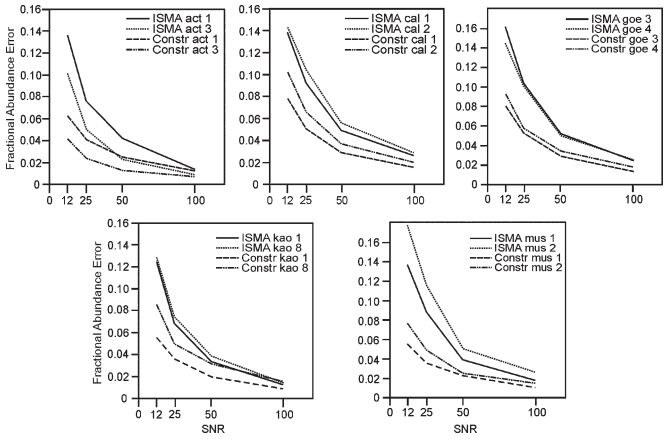

Fig. 9. Average fractional abundance error for mixtures containing multiple endmembers for the same mineral (refer to Table I). Act = actinolite, cal = calcite, goe = goethite, kao = kaolinite, and mus = muscovite.

< 0.05). For larger abundances (e.g., > 0.1), the error decreases and approaches that of the constrained unmixing method. This change in error as a function of actual abundance is not observed in the constrained unmixing results.

C. Results for the AVIRIS Cuprite Data Set

A total of 30 endmembers were extracted from the AVIRIS Cuprite data set using the IEA [20] extraction tool available in ISDAS [37]. Of the 30 endmembers, two were noisy spectra and were removed from the list. A shade endmember with a uniform reflectance of 1% absolute reflectance was used rather than the darkest pixel in the image, because the later had an average reflectance of 14% and a notable spectral shape. The remaining endmembers were used to unmix the data including spectra with similar overall shape but with subtle variations over specific spectral regions. For the Cuprite data, a number of Δrms threshold values were tested including the 5% value used for the simulated data. However, a Δrms threshold of 15% over two successive iterations was found to be more appropriate for the real data set.

A visual comparison of the fractional abundance maps generated using the ISMA and a fully constrained unmixing shows a similarity in the broad spatial distribution of abundance fractions with more noticeable differences occurring locally or between endmembers with similar spectral features (Fig. 10). The ISMA fractional abundance maps are also consistent with validated mineral maps produced using Tetracorder for the data set [38]. For the ISMA fractional abundance maps, 98.9% of the pixels are nonnegative and 93% sum to < 1.01 (excluding shade) (Fig. 11). Of the pixels that sum > 1.01, only 1.4% (3565 pixels) sum to > 1.1. Histograms of the fractional abundances for each endmember show that low abundance values dominate the fully constrained unmixing solution [Fig. 12(a)]. These low abundances are attributed to endmembers being used to improve the goodness of fit of the model, but these are likely not part of a given mixture. This is based on a knowledge of the spatial distribution and characteristics of the known minerals and mineral assemblages in the area derived from existing work, such as in [38]. For example, a number of

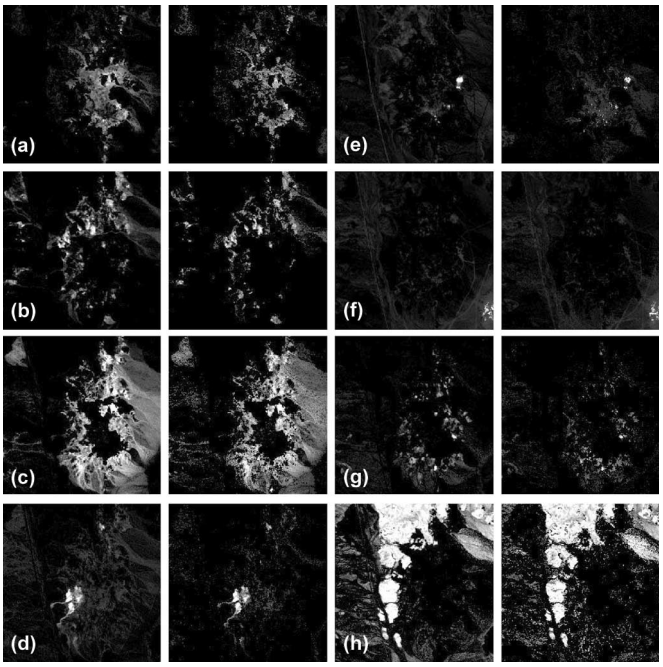

Fig. 10. Selected endmember fractional abundance maps for a subset of the image. (Left) Fully constrained unmixing and (right) ISMA. (a) Chalcedony 1, (b) Kaolinite, (c) Alunite 1, (d) Buddingtonite, (e) Chalcedony 2, (f) Montmorillonite, (g) Alunite 2, and (h) desert varnish. Images are linearly stretched from 0 to 0.5.

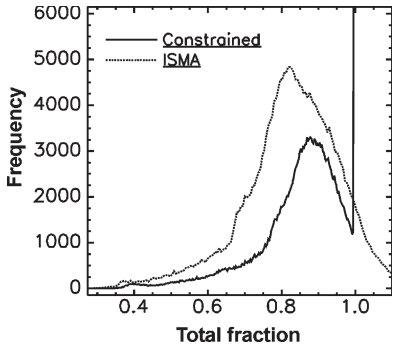

Fig. 11. Histogram showing the distribution of a total fractional abundance (excluding shade) for fully constrained and ISMA unmixing methods using the Cuprite hyperspectral data.

known minerals in the region are spatially confined to alteration zones (e.g., buddingtonite and chalcedony) and not distributed evenly throughout the image. Yet, the analysis of the abundance histograms and abundance images for fully constrained unmixing indicates a large number of pixels with low-abundance values (e.g., $< 10\%$) that are distributed outside these alteration zones. For fully constrained unmixing, 96% of the pixels are modeled by ≥ 5 endmembers in contrast with 37% using the IMSA. Fig. 12 also shows that the frequency distributions of endmember fractions are not truncated when calculated using the ISMA. For ISMA, multimodal distribution is observed, and there is also a distinctive shift to higher mean fractional abundances. This may be attributed to fewer endmembers being used to model each mixture, where each endmember contains a spectral information that is relevant to the given mixture.

Geological map units are defined in part based on characteristics of their mineralogy and mineral abundance. The fractional

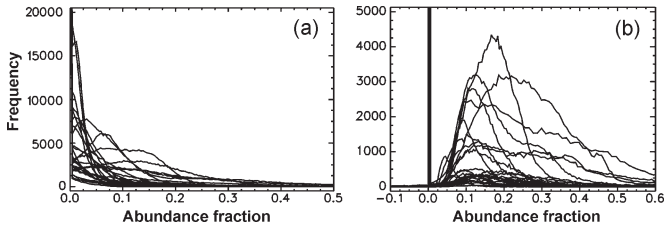

Fig. 12. Histograms of fractional abundance values for each endmember for (a) fully constrained and (b) ISMA unmixing results of the Cuprite data set. Note that vertical and horizontal scales are different for the two plots.

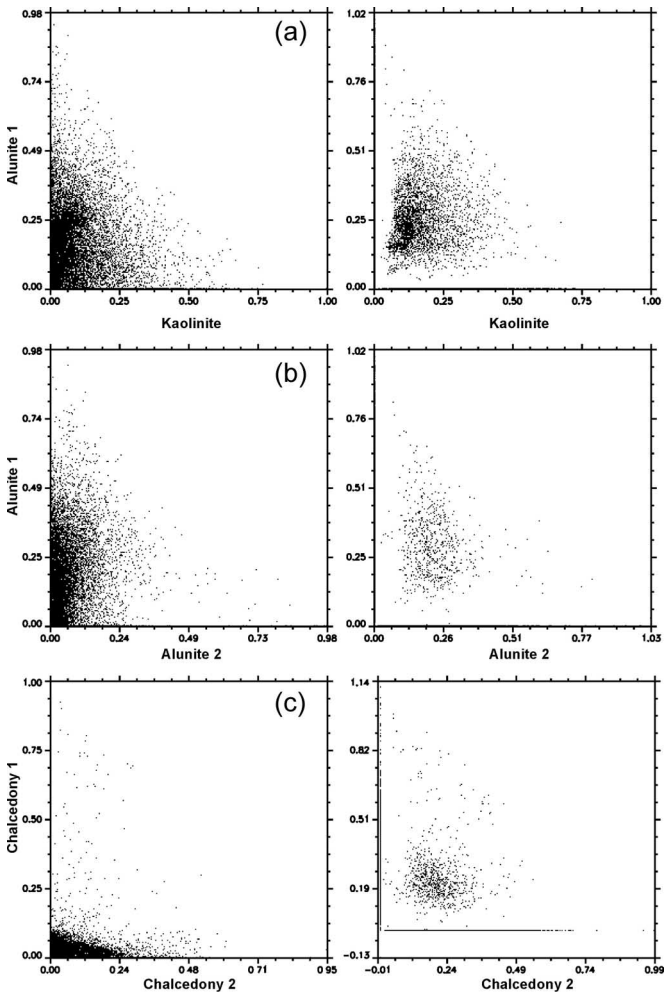

Fig. 13. Scatter plots of fractional abundances obtained using (left) fully constrained unmixing and (right) ISMA. (a) Kaolinite and Alunite 1, (b) Alunite 1 and 2, and (c) Chalcedony 1 and 2 (refer to Fig. 10). Note the vertical and horizontal scales in the left and right columns and ISMA results that include a few negative and > 1 values.

abundance maps show the nonrandom spatial distribution of minerals (Fig. 10). Scatter plots of fractional abundances for the selected region shown in Fig. 13 also reveal useful information for mapping, particularly for results obtained from the ISMA. In the case of the ISMA results, the scatter plots reveal clusters of pixels with similar mineral abundances corresponding to mappable units [e.g., Fig. 13(c)]. The same scatter plots for the fully constrained results lack well-defined clusters, and the abundances are predominantly low, reducing their value as a mapping tool.

VII. Discussion

The results of this study provide a comparison of per-pixel endmember sets and abundance determination obtained from the ISMA and other unmixing approaches. For the simulated data, the variable of greatest impact on each of the unmixing methodologies is an SNR, which is not unexpected. The ISMA outperformed the other methods at SNR $> 50:1$, a value exceeded by current airborne systems (e.g., AVIRIS, HyMAP), which have published an SNR averaging $> 1000:1$ in the visible and $> 500:1$ in the shortwave infrared [41], [42]. SNR for the Hyperion satellite hyperspectral sensor is as high as $100:1$ in the visible, but ranging from $50:1$ to $25:1$ in the shortwave infrared depending on the date of acquisition [41]. With an SNR approximating $50:1$, the ISMA should still be effective for selecting the optimal endmember set and reducing errors in fractional abundances. The simulated data results also indicate the impact of the number of endmembers that comprises a given mixture on the errors in the estimated fractional abundances. At SNR $> 50:1$, the ISMA has lower errors in fractional abundances if fewer than six endmembers comprise the mixture with the greatest improvement for 3–4 endmembers. The number of image endmembers comprising a pixel will fluctuate as a function of the scene and the spatial resolution of the image. However, it is reasonable to assume that this number will typically be less than seven endmembers (excluding shade), but likely closer to three or four. As such, the ISMA is particularly well suited to unmix the majority of pixels using existing hyperspectral sensors.

The ISMA exploits the characteristic variation in rms errors as a function of the numbers of endmembers utilized to solve a mixture. The rms error profiles have consistent characteristics independent of SNR, specifically the critical point that rarely corresponds to the lowest rms error. The consistent pattern of the rms-error profiles allows for a high degree of confidence in using the Δrms for selecting the critical point and, in turn, the optimal endmember set. However, based on the analysis of the simulated data, if endmembers have very low fractional abundances, the rms error increase after the critical point may be minimal and may impact the search for the critical point. In such circumstances, if the Δrms parameter is set too high, the ISMA will underestimate the number of endmembers. On the other hand, decreasing the Δrms may cause an overestimation of the number of endmembers in other mixtures. The parameters used for the simulated data gave accurate results, though on average slightly underestimated the number of endmembers. For the real data set, it was observed that a slightly higher Δrms performed best. Thus, further analysis is required to determine what parameters are optimal for most data sets. However, based on the design of ISMA, once an rms profile has been generated, multiple fractional abundance maps can be created for various Δrms without the necessity of repeating the iterative unmixing process.

The rms profiles also show that the rms error is low for the midrange of iterations prior to the critical point suggesting that the corresponding endmembers do not have a great influence on the modeled mixture but do minimize the rms error by adjusting for subtle spectral detail and noise. This characteristic may explain why the method used in [29] consistently overestimates the number of endmembers, where for each mixture, there exists a set of endmembers with positive fractional abundances that reduce the rms error but are not part of the mixture. If incorrect endmembers are retained, the error in fractional abundance increases for the correctly selected endmembers. Thus, we suggest that the critical point is a better representation of the optimal endmember set than just considering negative abundance fractions.

Determining the critical point from the rms profiles is computationally insignificant compared to the unmixing process. For ISMA, the computational load is controlled by the number of unconstrained unmixing iterations required to build the rms profile. Thus, the computational load is directly dependent on the number of endmembers in the given scene. This is also the case for MESMA, but as the number of endmembers increases, the number of mixing combinations increases substantially, whereas for ISMA, the increase is linear. In addition, the MESMA is affected by the number of endmembers comprising a pixel, such that if endmember combinations ≥ 4 (excluding shade) are required, the computational complexity becomes a burden. For ISMA, the number of endmembers in each pixel has no effect on computational efficiency. ISMA represents an alternative to MESMA, in which the ISMA has the capability of correctly selecting per-pixel endmember sets and producing accurate abundance fractions while at the same time significantly increasing computational efficiency and operational simplicity. It is noted here that the MESMA was originally designed to run using an appropriate endmember library derived from field and laboratory spectra [8], whereas the ISMA is designed to run using image endmembers.

Endmember extraction algorithms commonly retrieve a larger number of endmembers that include noisy spectra and spectra with similar overall shape. Noisy spectra are generally easy to identify and can be removed from the list. In the case of similar spectra, determining which endmembers should be retained for unmixing can be more problematic. Inherent to ISMA is its ability to complete this task automatically, but more importantly, it is designed to do this on a per-pixel basis.

Depending on the image, a complete endmember set may not be possible. Missing endmembers will have a similar effect on the ISMA rms profile as the removal of actual endmembers through the iterative process. However, the increase in rms attributed to the missing endmember will occur across the profile. Missing endmembers will likely reduce the fractional abundance accuracy regardless of the unmixing approach. Missing endmembers may in part explain the necessity in this study to increase Δrms for the real data. However, additional simulated tests are necessary to verify the full effects of missing endmembers.

In order to obtain physically realistic fractional abundances (nonnegative and summing to one), unmixing methodologies have focused on imposing ANC and ASC. However, using the ISMA, no constraints were required to obtain physically realistic fractional abundances for both the simulated and real data sets. This is a result of effectively selecting the optimal per-pixel endmembers sets and demonstrates the importance of using the correct endmembers to unmix individual pixels.

The results for the Cuprite data set are interesting in that both fully constrained and ISMA result in physically realistic abundance fractions (sum to one and nonnegative) and show similar map patterns of abundances, yet, the two differ with respect to abundance values and their histogram distributions. Most notable are two interrelated differences: 1) the number of endmembers used to model each pixel and 2) a shift to higher mean abundances for ISMA results. The first difference is key, in that for fully constrained unmixing, additional endmembers are used to reduce the residual error. This results in a high proportion of pixels with low abundance fractions. For ISMA, endmembers are only retained if their spectra contain information that can significantly reduce the rms error, which results in each endmember comprising a reasonable fraction of the mixture. Although the fractional abundances cannot be verified without ground truth data, the ISMA allows for a better discrimination of those endmembers that are likely to occur within a given pixel, as opposed to those that simply reduce the residual error. Selecting accurate per-pixel endmember sets is particularly important for minimizing errors in mapping. The abundance and presence of endmembers that comprise a large fraction of a given pixel are easily determined, but an endmember that comprises a small fraction of a pixel is more problematic, and its presence may be missed. These cases are of particular interest to users as the accurate selection of per-pixel endmember sets can significantly impact the ability to map the spatial distribution of an endmember of interest.

One topic that was not addressed in this study but should be briefly mentioned is the issue of endmember uniqueness and variability in the context of multispectral systems. For hyperspectral and multispectral systems, the number of possible unique endmembers is determined as the number of bands plus 1. For multispectral systems such as Landsat, which generally have less than seven statistically independent dimensions, the number of unique endmembers is restricted and will likely be fewer than what occurs in the scene. The forced restriction to a few spectral components does not allow for a proper consideration of the spectral variability related to intraclass differences. Thus, the solution for ISMA, as with any other unmixing algorithms, will be underdetermined.

VIII. Conclusion

The results of this study illustrate that the ISMA methodology developed in this paper is an effective tool to account for the per-pixel variability in image endmembers necessary to unmix individual pixels. Based on the analysis of simulated data, the method correctly selects the optimal endmember set 96% and 83.8% of the time for SNRs of $100:1$ and $12:1$, respectively. The accurate selection of an optimal endmember set at a high SNR ($100:1$) reduces errors in fractional abundances compared to that obtained from unmixing using the full endmember set. At an SNR of $> 50:1$, the ISMA produced results with fractional abundances that sum close to one and are not negative. Compared with an unconstrained unmixing, the ISMA significantly reduces fractional errors. The ISMA produces lower abundance errors compared with fully constrained unmixing for physically realistic mixtures (e.g., < 7 endmembers) at an SNR lower than that of available airborne sensors and consistent with that of satellite hyperspectral sensors. Compared with the method used in [29], the ISMA removes endmembers with low positive abundance fractions that are not part of a given mixture, thus minimizing false detection.

The results for the Cuprite data set show that both fully constrained and ISMA result in physically realistic abundance fractions with similar map patterns, yet they differ with respect to the abundance values and their detailed distribution. This difference is a result of ISMA only retaining endmembers that contain spectral information that is relevant to the given mixture and not noise. This impacts the ability to map the spatial distribution of an endmember of interest.

ISMA and MESMA are designed with the same objective in mind, with the key difference between the two being computational complexity. Although the MESMA has been shown to produce good results, the computational complexity of the method [8], [30]–[35] is a major drawback. The results from this study have demonstrated that selecting the correct per-pixel endmember set and producing accurate abundance fractions can be accomplished using the less computationally intensive ISMA method. It has also been shown that imposing constraints on the unmixing process to obtain physically realistic solutions is not a necessity if an accurate per-pixel endmember set is used. The ISMA method is straightforward, easy to implement, and has minimal user input.

Acknowledgment

The authors would like to thank K. Staenz (Canada Center for Remote Sensing) for access to ISDAS.

References

[1] J. J. Settle and N. A. Drake, "Linear mixing and the estimation of ground cover proportions," *Int. J. Remote Sens.*, vol. 14, no. 6, pp. 1159–1177, 1993.

[2] J. B. Adams, M. O. Smith, and P. E. Johnson, "Spectral mixture modeling: A new analysis of rock and soil types at the Viking Lander 1 site," *J. Geophys. Res.*, vol. 91, no. B8, pp. 8098–8112, Jul. 1986.

[3] J. B. Adams, M. O. Smith, and A. R. Gillespie, "Imaging spectroscopy: Interpretation based on spectral mixture analysis," in *Remote Geochemical Analysis: Elemental and Mineralogical Composition*, C. M. Pieters and P. A. Englert, Eds. Cambridge, U.K.: Cambridge Univ. Press, 1993, pp. 145–166.

[4] N. Keshava and J. F. Mustard, "Spectral unmixing," *IEEE Signal Process. Mag.*, vol. 19, no. 1, pp. 44–57, Jan. 2002.

[5] J. J. Settle, "On the relationship between spectral unmixing and subspace projection," *IEEE Trans. Geosci. Remote Sens.*, vol. 34, no. 4, pp. 1045–1046, Jul. 1996.

[6] D. C. Heinz and C.-I Chang, "Fully constrained least squares linear spectral mixture analysis method for material quantification in hyperspectral imagery," *IEEE Trans. Geosci. Remote Sens.*, vol. 39, no. 3, pp. 529–545, Mar. 2001.

[7] C. A. Bateson, G. P. Asner, and C. A. Wessman, "Endmember bundles: A new approach to incorporating endmember variability into spectral mixture analysis," *IEEE Trans. Geosci. Remote Sens.*, vol. 38, no. 2, pp. 1083–1094, Mar. 2000.

[8] D. A. Roberts, M. Gardner, R. Church, S. Ustin, G. Scheer, and R. O. Green, "Mapping chaparral in the Santa Monica Mountains using multiple endmember spectral mixture models," *Remote Sens. Environ.*, vol. 65, no. 3, pp. 267–279, Sep. 1998.

[9] D. E. Sabol, Jr., A. R. Gillespie, J. B. Adams, M. O. Smith, and C. J. Tucker, "Structural stage Pacific Northwest forests estimated using simple mixing models of multispectral images," *Remote Sens. Environ.*, vol. 80, no. 1, pp. 1–16, Apr. 2002.

[10] D. Lu, M. Batistella, E. Moran, and P. Mausel, "Application of spectral mixture analysis to Amazonian land-use and land cover classification," *Int. J. Remote Sens.*, vol. 25, no. 23, pp. 5345–5358, Dec. 2004.
[11] C. Small, "Estimation of urban vegetation abundance by spectral mixture analysis," *Int. J. Remote Sens.*, vol. 22, no. 7, pp. 1305–1334, May 2001.
[12] P. Bierwirth, R. Blewett, and D. Huston, *Finding New Mineral Prospects With HYMAP: Early Results From a Hyperspectral Remote-Sensing Case Study in the West Pilbara*, Nov. 1999. AGSO Research Newsletter 31. [Online]. Available: http://www.agso.gov.au/information/publications/resnews/
[13] G. P. Asner and K. B. Heidebrecht, "Spectral unmixing of vegetation, soil and dry carbon cover in arid regions: Comparing multispectral and hyperspectral observations," *Int. J. Remote Sens.*, vol. 23, no. 19, pp. 3939–3958, Oct. 2002.
[14] R. A. Neville, J. Levesque, K. Staenz, P. Nadeau, P. Hauff, and G. A. Borstad, "Spectral unmixing of hyperspectral imagery for mineral exploration: Comparison of results from SFSI and AVIRIS," *Can. J. Remote Sens.*, vol. 29, no. 1, pp. 99–110, 2003.
[15] J. W. Boardman, "Automating spectral unmixing of AVIRIS data using convex geometry concepts," in *Proc. Summ. 4th Annu. JPL Airborne Geosci. Workshop*, 1993, vol. 1, pp. 11–14, JPL Publ. 93-26.
[16] A. Bateson and B. Curtiss, "A method for manual endmember selection and spectral unmixing," *Remote Sens. Environ.*, vol. 55, no. 3, pp. 229–243, Mar. 1996.
[17] M. E. Winter, "Fast autonomous spectral endmember determination in hyperspectral data," in *Proc. 13th Int. Conf. Appl. Geologic Remote Sens.*, Vancouver, BC, Canada, 1999, vol. II, pp. 337–344.
[18] J. Bowles, P. J. Palmadesso, J. A. Antoniades, M. M. Baumback, and L. J. Rickard, "Use of filter vectors in hyperspectral data analysis," in *Proc. SPIE Infrared Spaceborne Remote Sens. III*, 1995, pp. 148–157.
[19] A. Ifarraguerri and C.-I Chang, "Multispectral and hyperspectral image analysis with convex cones," *IEEE Trans. Geosci. Remote Sens.*, vol. 37, no. 2, pp. 756–770, Mar. 1999.
[20] R. A. Neville, K. Staenz, T. Szeredi, J. Lefebvre, and P. Hauff, "Automatic endmember extraction from hyperspectral data for mineral exploration," in *Proc. 4th Int. Airborne Remote Sens. Conf. and Exhib./21st Can. Symp. Remote Sens.*, Ottawa, ON, Canada, Jun. 21–24, 1999, pp. 891–896.
[21] A. Plaza, P. Martinez, R. Perez, and J. Plaza, "Spatial/spectral endmember extraction by multidimensional morphological operations," *IEEE Trans. Geosci. Remote Sens.*, vol. 40, no. 9, pp. 2025–2041, Sep. 2002.
[22] M. Berman, H. Kiiveri, R. Lagerstrom, A. Ernst, R. Dunne, and J. F. Huntington, "ICE: A statistical approach to identifying endmembers in hyperspectral images," *IEEE Trans. Geosci. Remote Sens.*, vol. 42, no. 10, pp. 2085–2095, Oct. 2004.
[23] J. M. P. Nascimento and J. M. B. Dias, "Vertex component analysis: A fast algorithm to unmix hyperspectral data," *IEEE Trans. Geosci. Remote Sens.*, vol. 43, no. 4, pp. 898–910, Apr. 2005.
[24] A. R. Gillespie, "Spectral mixture analysis of multispectral thermal infrared images," *Remote Sens. Environ.*, vol. 42, no. 2, pp. 137–145, Nov. 1992.
[25] D. E. Sabol, J. B. Adams, and M. O. Smith, "Quantitative sub-pixel spectral detection of targets in multispectral images," *J. Geophys. Res.*, vol. 97, no. E2, pp. 2659–2672, Feb. 1992.
[26] M. Petrou and P. G. Foschi, "Confidence in linear spectral unmixing of single pixels," *IEEE Trans. Geosci. Remote Sens.*, vol. 37, no. 1, pp. 624–626, Jan. 1999.
[27] S. Roessner, K. Segl, U. Heiden, and H. Kaufmann, "Automated differentiation of urban surfaces based on airborne hyperspectral imagery," *IEEE Trans. Geosci. Remote Sens.*, vol. 39, no. 7, pp. 1525–1532, Jul. 2001.
[28] H. Gross, "An image fusion algorithm for spatially enhancing spectral mixture maps," Ph.D. dissertation, U.S. Air Force, Rochester Inst. Technol., New York, 1996.
[29] M. S. Ramsey and P. R. Christensen, "Mineral abundance determination: Quantitative deconvolution of thermal emission spectra," *J. Geophys. Res.*, vol. 103, no. B1, pp. 577–596, Jan. 1998.
[30] W. J. Okin, G. S. Okin, D. A. Roberts, and B. Murray, "Multiple endmember spectral mixture analysis: Endmember choice in an arid shrubland," in *Proc. AVIRIS Workshop*, R. O. Green, Ed, Pasadena, CA, 1999, pp. 323–332.
[31] L. Li and J. F. Mustard, "Highland contamination in lunar mare soils: Improved mapping with multiple end-member spectral mixture analysis (MESMA)," *J. Geophys. Res.*, vol. 108, no. E6, 5053, pp. 7-1–7-14, 2003.
[32] D. A. Roberts, P. E. Dennison, M. Gardner, Y. L. Hetzel, S. L. Ustin, and C. Lee, "Evaluation of the potential of Hypersion for fire danger assessment by comparison to the Airborne Visible Infrared Spectrometer," *IEEE Trans. Geosci. Remote Sens.*, vol. 14, no. E6, pp. 1297–1310, Jun. 2003.
[33] G. S. Okin, D. A. Roberts, B. Murray, and W. J. Okin, "Practical limits on hyperspectral vegetation discrimination in arid and semiarid environments," *Remote Sens. Environ.*, vol. 77, no. 2, pp. 212–225, Aug. 2001.
[34] T. H. Painter, J. Dozier, D. A. Roberts, R. E. Davis, and R. O. Green, "Retrieval of subpixel snow-covered area and grain size from imaging spectrometer data," *Remote Sens. Environ.*, vol. 85, no. 1, pp. 64–77, Apr. 2003.
[35] P. E. Dennison and D. A. Roberts, "Endmember selection for multiple endmember spectral mixture analysis using endmember average RMSE," *Remote Sens. Environ.*, vol. 87, no. 2/3, pp. 123–135, Oct. 2003.
[36] K. H. Haskell and R. J. Hanson, "An algorithm for C linear least squares problems with equality and C nonnegativity constraints," *Math. Program.*, vol. C21, no. 1, pp. 98–118, Dec. 1981.
[37] K. Staenz, T. Szeredi, and J. Schwarz, "ISDAS—A system for processing/analyzing hyperspectral data; Technical note," *Can. J. Remote Sens.*, vol. 24, no. 2, pp. 99–113, 1998.
[38] R. N. Clark, G. A. Swayze, K. E. Livo, R. F. Kokaly, S. J. Sutley, J. B. Dalton, R. R. McDougal, and C. A. Gent, "Imaging spectroscopy: Earth and planetary remote sensing with the USGS Tertracorder and expert systems," *J. Geophys. Res.*, vol. 108, no. E12, pp. 5-1–5-44, 2003.
[39] R. N. Clark, G. A. Swayze, A. J. Gallagher, T. V. V. King, and W. M. Calvin, "The U.S. Geological survey, digital spectral library: Version 1: 0.2 to 3.0 microns," U.S. Geol. Surv., Denver, CO, USGS Open File Rep. 93-592, 1993.
[40] J. C. Harsanyi and C. I Chang, "Hyperspectral image classification and dimensionality reduction: An orthogonal subspace projection approach," *IEEE Trans. Geosci. Remote Sens.*, vol. 32, no. 4, pp. 779–785, Jul. 1994.
[41] F. A. Kruse, "Comparison of AVIRIS and Hyperion for hyperspectral mineral mapping," in *Proc. 11th JPL Airborne Geosci. Workshop*, Pasadena, CA, Mar. 4–8, 2002. JPL Publ. 03-4 (CD-ROM).
[42] T. Cocks, R. Jensen, A. Stewart, I. Wilson, and T. Shields, "The HYMAP Airborne hyperspectral sensor: The system, calibration and performance," in *Proc. 1st EARSEL Workshop Imag. Spectroscopy*, Zurich, Switzerland, Oct. 1998, pp. 37–42.

Derek M. Rogge received the B.S. (Hons.) and M.Sc. degrees in geology from the University of Manitoba, Winnipeg, MB, Canada, in 1998 and 2002, respectively. He is currently working toward the Ph.D. degree at the University of Alberta, Edmonton, AB, Canada.

He has been involved with collaborative projects with the Manitoba Geological Survey, Geological Survey of Canada, and the Institute for Aerospace Research, National Research Council of Canada. His current research is focused on the application of hyperspectral data for geological mapping in the Canadian Arctic, specifically the problems related to spectral unmixing and the integration of spatial and spectral information for mapping.

Benoit Rivard received the Ph.D. degree in earth and planetary sciences from Washington University, St. Louis, MO, in 1990.

He is currently a Professor with the Department of Earth and Atmospheric Sciences, University of Alberta, Edmonton, AB, Canada. His past research interests have included the use of ground and airborne multispectral remote sensing for lithologic and structural mapping, the infrared characterization of terrestrial materials, the development of methodologies for precise measurement of emissivity, and the analysis of radar data for regional geologic mapping. Currently, much of his research is applied and driven by interactions with industrial collaborators of resource industry, specifically the mining exploration sector. Projects include the pursuit of underground telemining operations for wall rock mapping, ore estimation, and core logging. This research is generating promising results for automation and improving the scientific understanding of the visible, near-infrared, and thermal infrared scattering properties of ore minerals, and of broken and cut rock surfaces in general. In addition, analysis tools dedicated to these applications are being designed. He is also involved in an investigation of the spectral properties of silica spring deposits as a potential reservoir for fossil life on Mars and is exploring the means of detecting these materials from spectral data.

Dr. Rivard is a member of the National Hyperspectral User and Science Team, which is an advisory panel to the Canadian Space Agency for their hyperspectral satellite development program.

Jinkai Zhang received the B.S. degree in geology from Peking University, Beijing, China, in 1990, the M.S. degree from the Institute of Remote Sensing Applications (IRSA), Chinese Academy of Sciences (CAS), Beijing, in 1993, and the Ph.D. degree from the University of Alberta, Edmonton, AB, Canada, in 2004.

From 1993 to 1999, he was a Research Assistant with IRSA, CAS, focusing on the application of multispectral remote sensing for mapping mineralization and thermal infrared spectroscopy of minerals/rocks. He is currently working as a Postdoctoral Fellow with the Department of Earth and Atmospheric sciences, University of Alberta. His current research is focused on the spectral analysis of hyperspectral data for geological applications, including spectral mixture analysis for rock/mineral abundance estimates, derivative analysis to extract subtle rock spectral signatures, the deconvolution of lichen-rock mixtures to facilitate detailed lithologic mapping, and spectral normalization to suppress intraclass spectral variations.

Jilu Feng received the M.S. degree in cartography and remote sensing from Peking University, Beijing, China, in 1991, and the Ph.D. degree in earth and atmospheric sciences from the University of Alberta, Edmonton, AB, Canada, in 2002.

His research interests include the use of multispectral and hyperspectral data for lithology and mineral mapping, SAR characterization of terrestrial materials, and the development of methodologies and new algorithms for target detection. His current research projects include automatic rock-type identification in core logging from hyperspectral devices and the rapid characterization of oil sand from reflectance spectroscopy.